THERMOELECTRIC PROPERTIES OF POLYSILICON INVERSE OPALS

BY

JUN MA

THESIS

Submitted in partial fulfillment of the requirements
for the degree of Master of Science in Mechanical Engineering
in the Graduate College of the
University of Illinois at Urbana-Champaign, 2012

Urbana, Illinois

Adviser:

Professor Sanjiv Sinha

ABSTRACT

Nanostructured single-crystal silicon exhibits a remarkable increase in the figure of merit for thermoelectric energy conversion. Here we theoretically and experimentally(partial) investigate a similar enhancement for polycrystalline silicon structured as an inverse opal. An inverse opal provides nanoscale grains and a thin-film like geometry to scatter phonons preferentially over electrons. Using solutions to the Boltzmann transport equation for electrons and phonons, we show that the figure of merit at 300 K is fifteen times that of bulk single-crystal silicon. Our models predict that grain boundaries are more effective than surfaces in enhancing the figure of merit. We provide insight into this effect and show that preserving a grain size smaller than the shell thickness of the inverse opal increases the figure of merit by as much as 50% when the ratio between the two features is a third. At 600 K, the figure of merit is as high as 0.6 for a shell thickness of 10 nm. We also measured the thermal conductivity of such nanostructures, and a more accurate thermal transport model is provided based on the experimental results.

To my parents, for their love and support.

ACKNOWLEDGMENTS

I would like to express my gratitude to my advisor Professor Sanjiv Sinha, who allowed me to choose the topic I am interested in and guided me through the research work from scratch. I am extremely grateful to Prof. Sinha for his patience and encouragement during the difficult times in my research. His advise on personal development and understanding of my situation as an international students have been of tremendous help.

This work could not be finished without my collaborators. Special acknowledgements to Marc Ghossoub, who helped me begin and pursue successfully a great deal of the project. I would wish to thank Dr. Agustin Mihi and Bibek Parajuli in MatSE department for providing the samples for the measurement. I owe my thanks to Jyothi Sadhu, who has shared a lof of ideas on phonon transport with me. And Krishna Valavala, who shared the experimental set up with me and spent most of the course work time together. Finally, I want to thank all the members in my group, for the joy I have been enjoying over the last two year working with them.

TABLE OF CONTENTS

LIST OF FIGURES

CHAPTER 1

INTRODUCTION

1.1 Background and General Concepts

The efficiency of energy conversion in a thermoelectric material depends on the thermoelectric figure of merit, ZT where T is the absolute temperature and Z is a material parameter equal to $S^2\sigma_{\text{effec}}/\kappa_{\text{effec}}$. Here S is the Seebeck coefficient, σ_{effec} is the effective electrical conductivity and κ_{effec} is the effective thermal conductivity. A reduction in thermal conductivity enhances the figure of merit for thermoelectric materials [1, 2, 3, 4, 5]. Nanostructures, in particular, facilitate such reduction [3], mostly through phonon boundary scattering. A striking example is single-crystal silicon whose figure of merit increases fifty times compared to the bulk when structured in the form of nanowires[6, 7] or membranes with arrays of holes [8, 9]. In this thesis, we show that similar enhancement in the figure of merit is possible in polysilicon structured in the form of an inverse opal. The structure we propose has the advantages of lower material cost and a thin-film geometry that enables better device engineering.

Inverse opals [10](Figure 1.1) are a class of self-assembled colloidal structures [11, 12] where material is deposited in the interstices of a colloidal crystal followed by removal of the original template. These structures attract interest in photonics where their three-dimensional periodicity creates complete photonic band gaps in certain cases [13]. The phenomena we seek to exploit here does not depend on band gaps but rather on scattering. The large surface area to volume ratio and small grain size available in inverse opals facilitates enhanced phonon scattering. These processes also affect electron transport but to a lesser extent. In typical applications, the thermoelectric material is doped to reduce its resistivity to $\sim$mΩ-cm. At such doping, the electron mean free path in silicon is $\lesssim$10 nm at room

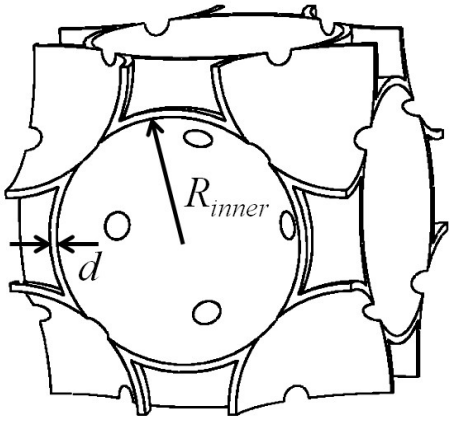

Figure 1.1: The schematic of an inverse opal unit cell.

temperature and largely dominated by impurity scattering.

Previous theoretical work on the thermoelectric properties of regular opals suggests that there is no enhancement in the figure of merit compared with the bulk. Sofo and Mahan [14] modeled conduction in a regular opal as a random walk in a lattice, with residence time within sites. This gives rise to a linear relation between the carrier mean free path and the diffusion coefficient, such that the opal preserves the figure of merit of the bulk material. Unlike opals, diffusion in inverse opals is not a site hopping phenomena but is instead, related to transport along continuous thin sections containing grain boundaries. We show that this partially decouples charge and heat transport with a net enhancement in the figure of merit.

The opal geometry modifies flow fields such that the effective conductivity of an inverse opal thin-film is different from the intrinsic conductivity. However, the ratio of the effective electrical to thermal conductivity is the same as the ratio of the intrinsic material conductivities, since electrical and thermal flow fields remain similar inside an inverse opal [15]. Thus, the geometry in itself does not affect the figure of merit in the continuum limit.

The overall resistance posed by the structure does depend on geometry as emphasized above. The relation between the effective conductivity and the intrinsic conductivity can deviate substantially from the effective medium theory [16, 17] at large porosities or in the case of large differences in conductivities between air and the solid comprising the inverse opal. The inverse opal of interest here has a face-centered cubic (FCC) lattice. Figure 1.1 shows the schematic of an inverse opal. Typical inverse opals made from self-assembled oxide

spheres, possess shell thickness, d in the range ∼15–35 nm and inner diameters, R_{inner} in the range ∼100–300 nm [12]. The relationship between the inner diameter of the sphere and the shell thickness is well defined if the pores in the opal structure are filled to the maximum at 86% [18]. The FCC opal has a filling factor of 74%, and the maximum filling factor of the inverse opal is 86%×(1-0.74)≅22%. Using this figure, d is approximately equal to 9.2% of R_{inner} if we ignore the holes in Figure 1.1 and is equal to 12% of R_{inner} [18] if we account for the presence of these holes. In either case, we expect porosities exceeding 0.75 and cannot employ the effective medium approximation to estimate the effective conductivities. We use instead the relations provided by a boundary integral solution to the flow fields [15]. At the theoretical minimum porosity of ∼ 78%, the effective conductivity is ∼11.5% of the intrinsic material conductivity.

1.2 Structure of the Thesis

The rest of the thesis is organized as follows.

In Chapter 2 we theoretically investigate the individual behaviors of thermal conductivity, electrical conductivity and the Seebeck coefficient in polysilicon inverse opals as a function of shell thickness and grain size. We consider detailed electron scattering mechanisms to investigate charge transport. In modeling phonon transport, we pay special attention to phonon-electron scattering and propose an improved model compared to the existing literature. Our work provides insight into the relative effects of surface and grain boundary scattering on thermoelectric properties. We estimate the figure of merit for polysilicon inverse opals to be as high as 0.15 at 300 K and ∼0.6 at 600 K, comparable to recently reported thin film thermoelectric materials [19] that are more complex and expensive to manufacture.

In Chapter 3 we present the thermal conductivity measurements of 3 samples with different shell thicknesses but fabricated in the same manner. We employed the 3ω [20] method to do the measurement and went down to as low as 15 K. The thermal conductivity measurement advances the understanding of phonon transport in extremely porous structure. It also provides useful information in various applications that utilizes such structure, e.g. the emitter in a solar cell.

Finally, we summarize the theoretical and experimental findings in Chapter 4.

CHAPTER 2

THEORETICAL MODELING

In this chapter, we use the relation between the effective conductivity and the intrinsic material conductivity but modify the intrinsic conductivity from the bulk to account for sub-continuum transport. In effect, we assume that the inverse opal geometry affects transport at continuum scales but does not affect transport at sub-continuum scales. We justify this approach based on the dimensions of the opals under consideration. Inverse opals of interest possess shell thicknesses comparable to the carrier mean free paths. However, the particle diameter is substantially larger than the mean free path. Thus, the geometry for solving the Boltzmann equation reduces from that of the inverse opal to that of a regular thin film. Details such as curvature of the segments are ignored in the sub-continuum solution and accounted for in the continuum solution. We model charge and heat transport to obtain the intrinsic material properties of an inverse opal below.

2.1 Thermoelectric Properties

In this section, we compute the intrinsic electrical conductivity, thermal conductivity and Seebeck coefficient of a polysilicon inverse opal. Previous theoretical work[21, 22, 23, 24, 25] has considered charge conduction in bulk polysilicon in great detail. Here, we consider energy dependent relaxation times and employ a distribution function that accounts for both film thickness and grain boundaries. We also obtain the diffusion and phonon-drag components of the Seebeck coefficient directly from the solution to the Boltzmann equation in a thin film geometry while accounting for grain boundaries. In considering thermal transport, we make several modifications compared to the existing literature on modeling polysilicon [26] to improve the accuracy of predictions. Specifically, we propose a new model for phonon-

electron scattering based on deformation potentials.

2.1.1 Electrical Conductivity

Charge transport in an inverse opal occurs along the interstices of the original opal. The diameter of the colloidal particles forming the opal are typically 200–600 nm [12] and the interstices have thickness in the range 15–35 nm. We assume the inverse opal to be perfect, yielding continuously joined interstices. The thickness of these thin segments is comparable to the carrier mean free paths and the boundaries are expected to alter the carrier distribution as is typical in thin films. We neglect the effect of the curvature since this is relatively small compared to the effect of the shell thickness. We note that this may not necessarily be the case with inverse opals formed from much smaller particles ($\leq$50 nm).

The problem reduces to charge transport in a thin, polycrystalline film with background scattering processes. We model such a film along the lines proposed by Mayadas and Shatzkes [27]. We summarize the main idea here for the sake of completeness. In this approach, a δ-function represents a columnar grain boundary and perturbation theory provides the wave vector dependent relaxation time as

$$\tau_{\text{e-g}}^{-1} = \frac{v_{\text{e}}}{l}\frac{R}{1-R}\frac{k}{|k_x|}\cdot\frac{1-e^{-4k_x^2s^2}}{1+e^{-4k_x^2s^2}-2e^{-k_x^2s^2}\cos(2k_xl)}, \tag{2.1}$$

where k and v_{e} are the wavevector and the speed of electron, R is the reflection coefficient, taken to be 1/2, l and s are average grain size and standard deviation. We obtain the latter from a normal distribution fit to the data in Ref.[28] and find this to be 1/3 of l. We further integrate the relaxation time over different directions in k-space to obtain an energy dependent $\tau_{\text{e-g}}^{-1}(E)$.

Considering an electron confined along the $z-$direction by the film thickness, d and traveling in the presence of an electrical field $\overrightarrow{\mathcal{E}}$ and a temperature gradient ∇T, both transverse to the film thickness and along the $x-$direction, the Boltzmann transport equation is

$$v_z\frac{\partial f_1}{\partial z} - e\mathcal{E}v_x\frac{\partial f_0}{\partial E} + v_x\frac{\partial f_0}{\partial x} = \frac{f_1}{\tau^*(E)}, \tag{2.2}$$

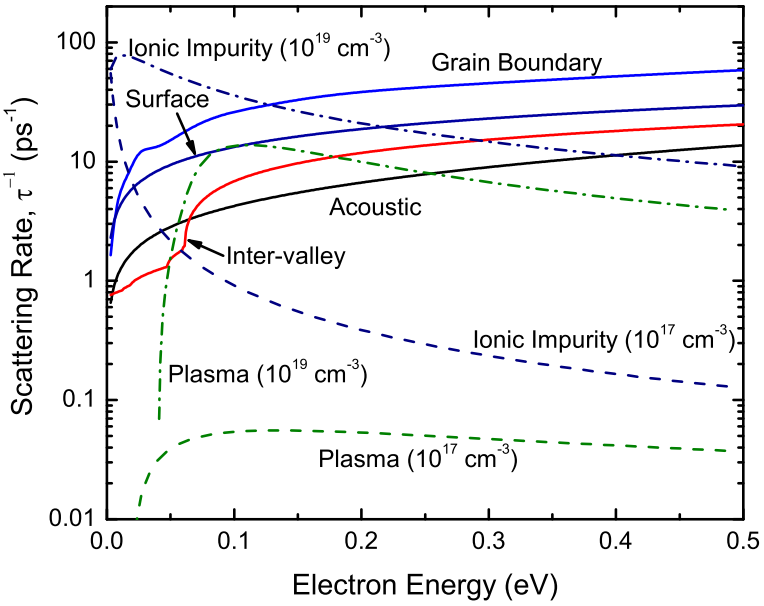

Figure 2.1: Scattering rates of electrons for different processes in silicon at 300 K. Solid lines represent scattering mechanisms insensitive to doping. Dashed and dot-dashed lines represent doping levels of 10^{17} cm^{-3} and 10^{19} cm^{-3} respectively. The shell thickness and average grain size are both 25 nm.

where f_1 is the deviation from the equilibrium distribution f_0, that arises due to confinement along z. The temperature gradient is set to zero in the electrical conductivity calculation, such that $\partial f_0/\partial x$ vanishes. We note that τ^* is an energy dependent background relaxation time in our work and is not a constant as originally considered by Mayadas and Shatzkes [27]. Using Matthiessen's rule, the background relaxation rate is related to individual relaxation rates as $\tau^{*-1} = \sum \tau_i^{-1}$, where i represents electron-phonon, electron-impurity, electron-electron, and plasmon scattering. We use deformation potentials [29] to model intravalley and intervalley phonon scattering. Following Fischetti [30], we use the Brooks-Herring formula [31] to compute the relaxation time due to ionic impurities. We account for phase shift [32] at doping levels greater than 10^{17} cm^{-3} to correct the Born approximation in the Brooks-Herring formula. Electron-electron scattering does not affect mobility directly, as momentum is transferred between electrons. This, however, modifies the energy distribu-

tion and is accounted for in our calculations [32]. Finally, we follow Fischetti [30] in the treatment of plasmon scattering. Figure 2.1 plots different scattering rates as a function of the electron energy. We include a simplistic boundary scattering rate, $\tau_{\text{e-b}}^{-1} = v/d$ here for comparison. We discard this in favor of the exact Boltzmann solution when calculating mobility below. The figure plots ionic impurity and plasma scattering rates at two different impurity concentrations to illustrate the dependence of doping.

By applying boundary conditions, Eq. 2.2 is solved as

$$f_1 = \begin{cases} -e\mathcal{E}\tau^* v_x \dfrac{\partial f_0}{\partial E}\left[1 - e^{-z/v_z\tau^*}\right], v_z > 0 \\ -e\mathcal{E}\tau^* v_x \dfrac{\partial f_0}{\partial E}\left[1 - e^{(d-z)/v_z\tau^*}\right], v_z < 0 \end{cases} \tag{2.3}$$

for purely diffuse surface scattering. The current density $J_x(z)$ is then

$$J_x(z) = -\frac{1}{4\pi}\int_0^\infty \int_0^{2\pi} \int_0^\pi f D(E) e v_x \sin\theta d\theta d\varphi dE. \tag{2.4}$$

Here $f = f_0 + f_1$ is the total distribution function, $D(E) = E^{1/2}[3(2m)^{3/2}]/(\pi^2\hbar^3)$ is the density of states assuming parabolic bands. The density-of-states effective mass, m of a single valley is $0.32\,m_0$ where m_0 is the rest mass of a free electron.We use the conductivity effective mass, $m_{\text{c}} = 0.26\,m_0$ in converting the electron velocity to energy in Eq. 2.4. The electrical conductivity and mobility are respectively $\sigma = 1/(\mathcal{E}d)\int_0^d J_x(z)dz$ and $\mu = \sigma/(en)$, where n is the electron number density.

Figure 2.2 plots the resulting mobility in a polysilicon inverse opal as a function of doping. The shell thickness and grain size are both 25 nm. We report calculations on bulk single-crystal, thin-film single-crystal, and bulk polysilicon for comparison. The agreement with the data for single-crystal bulk silicon is good as expected. We now turn our attention to polysilicon. Dopant segregation is an important factor in the mobility of polysilicon, which in turn depends strongly on the doping method [35] and annealing conditions [36]. Ion implantation introduces dopant segregation at the grain boundaries [36] while in-situ doping [37] appears to avoid this. Since inverse opals must be doped in-situ, data from in-situ doped polysilicon samples provide the right comparison. The measured mobility [37] in polysilicon

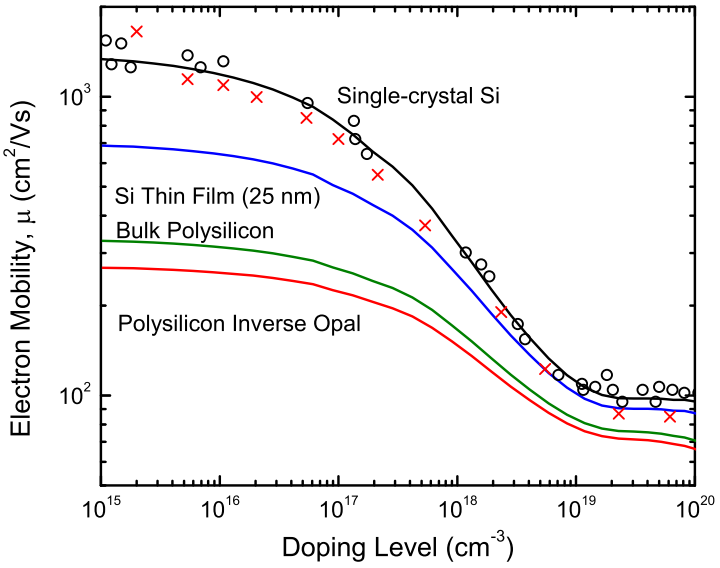

Figure 2.2: Electron mobility in bulk and thin-film single-crystal silicon, bulk polysilicon and polysilicon inverse opals at 300 K. The shell thickness and grain size are both 25 nm. The data are from Ref. [33] (open circles) and Ref. [34] (crosses).

nanowires doped with phosphorus at 3×10^{19} cm^{-3} and 2×10^{20} cm^{-3} are respectively 69 cm^2/Vs and 25 cm^2/Vs, comparable with our calculated values. The measurements did not include characterization of grain size. However, since the samples were annealed at a low temperature (600^{0}C for 12 hours), we expect small grains. Siebe et al. [38] also reported similar mobility for in-situ phosphorus doped polysicon at 2×10^{20} cm^{-3}, with average grain size of 20–30 nm. Our calculations are thus consistent with the limited set of data available in the literature.

Our calculations show that while surface and grain boundary scattering reduce mobility significantly at low doping, the reduction is $\sim 30\%$ above doping levels of 10^{19} cm^{-3} when the average grain size and shell thickness are both 25 nm. Overall, the electrical conductivity reduces by $\sim$92% of the bulk value. A larger part of the reduction stems from geometry that affects flow fields. We note that we have ignored any deactivation of donors in these calculations. Deactivation arises from reduced screening of the impurity potential due to low dielectric constant of the surroundings. In silicon nanowires, for example, significant

deactivation occurs [39] at diameters less than 20 nm, when the doping level is 3×10^{19} cm^{-3}. Given the thin film geometry, we expect this deactivation to occur at even smaller dimensions in inverse opals and neglect it in our work.

2.1.2 Thermal Conductivity

The lattice thermal conductivity of polysilicon can be expressed as

$$\kappa = \frac{1}{3}\frac{1}{2\pi^2 k_B T^2}\sum_{\lambda}\int_0^{q_c}\frac{(\hbar\omega)^2\omega^2 e^{\hbar\omega/k_B T}}{\left[e^{\hbar\omega/k_B T}-1\right]^2}\tau(q)dq, \tag{2.5}$$

where λ represents different phonon polarizations, k_B is the Boltzmann constant, $\hbar$ is the reduced Planck's constant, and q is the phonon wave number. In this paper, we use the linear dispersion relation proposed by Holland [40] that fits the thermal conductivity data for bulk silicon reasonably well. The phonon frequency, ω is given by $\omega = v_\lambda q$, where v_λ is the phonon propagation speed.

The thermal conductivity of doped polysilicon is extensively studied in the literature [26]. Scattering mechanisms of interest include Umklapp scattering, isotope and impurity mass difference scattering, surface and grain boundary scattering, and phonon-electron scattering. We use scattering rates from the literature [41] for Umklapp and mass difference scattering. These are of the form $\tau_u^{-1} = BT\omega^2 e^{-C/T}$, and $\tau_m^{-1} = V_0\Gamma/(4\pi v_s^3)\omega^4$, where $B = 1.9 \times 10^{19}$ s/K, $C = 160$ K are constants determined from bulk thermal conductivity data, v_s is sound velocity, V_0 is the volume per atom, and Γ is defined as $\Gamma = \sum_j f_j(1 - M_j/\overline{M})^2$. Here, f_j is the percentage of atom type j, whose mass is M_j, and $\overline{M}$ is the average atomic mass. The effect of both isotope and impurity scattering can be evaluated using this equation.

We use a frequency dependent[42] grain boundary scattering rate,

$$\tau_{p\text{-}g}^{-1} = \frac{v_s}{\alpha l}\frac{\omega}{\gamma\omega_c}. \tag{2.6}$$

where α, γ are dispersion dependent constants [42], ω_c is the cut-off frequency for each linear segment in Holland's [40] dispersion. We use $\tau_{p\text{-}b}^{-1} = v_s/Fd$ as the boundary scattering rate, where F is a geometric parameter.

With the high doping required in thermoelectric applications, phonon-electron scattering, which is otherwise neglected, assumes importance. In modeling the thermal conductivity of doped polysilicon films, Asheghi et al. [43] employed a deformation potential to calculate the phonon-electron interaction. However, the deformation potential was fit at each doping level, which reduces the physical significance of the model. In a different paper, Zou [44] assumed the scattering rate to be linear in the carrier concentration, which is only valid at low doping levels. Here we develop a new expression that accounts for low as well as high doping.

We start with the transition rate used in the calculation of electron relaxation time due to phonon scattering [45]:

$$S(\mathbf{p},\mathbf{p}') = \frac{\pi m {D_{\mathrm{A}}}^2}{\hbar \rho v_{\mathrm{s}} p V} \delta\left(\pm cos\theta + \frac{\hbar q}{2p} \mp \frac{\omega}{v_{\mathrm{e}} q}\right), \tag{2.7}$$

where $\mathbf{p}$, $\mathbf{p}'$ are the momentum of an electron before and after scattering, θ is the angle between the two directions, D_{A} is the magnitude of the deformation potential, ρ is the density of silicon, and V is a normalization volume. The δ-function ensures momentum and energy conservation. High frequency phonons are unlikely to be scattered as electrons in the conduction band of n-type silicon are only thermally excited and do not possess sufficient energy. Due to symmetry, only longitudinally polarized phonons scatter electrons [46].

Instead of summing over the phonon wave number as in the case of electron transport, we sum the transition rate over spins, valleys and all final electronic states to evaluate the phonon relaxation time due to electron scattering,

$$\tau_{\text{p-e}}^{-1} = \sum_{\uparrow, valley, \mathbf{p}'} S(\mathbf{p},\mathbf{p}') f(\mathbf{p})(1 - f(\mathbf{p}')). \tag{2.8}$$

Here, $f(\mathbf{p})$ is the probability of an available electron to be scattered while $(1 - f(\mathbf{p}'))$ is the probability of availability of the final state to be scattered into. Noting that electrons have the same spin and remain in the same valley before and after the scattering process, summations over spins and valleys give degeneracies of 2 and 6 respectively. After the summation, $\tau_{\text{p-e}}$ is only a function of the phonon wave number q.

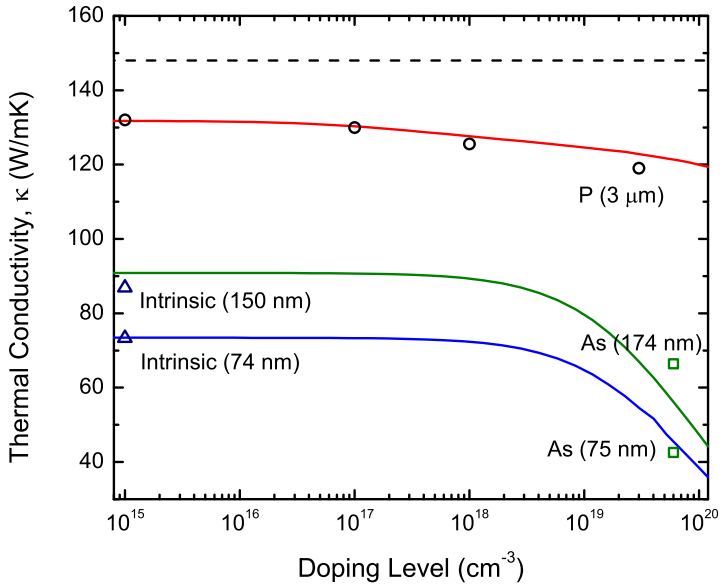

Figure 2.3: Thermal conductivity as a function of doping concentration at 300 K. The open circles, triangles and squares are measurement values from Ref. [43, 47, 48]. The red, green and blue curves are calculations for P-doped 3 μm thick, As-doped 174 nm thick, and As-doped 74 nm thick single-crystal silicon films respectively.

We set the deformation potential, D_{A} to 9 eV, which is the value determined from fits to mobility data[29]. Figure 2.3 compares the available experimental data for n-doped silicon films with calculations. The predictions agree well with the data which, however, are a limited set. We note that the agreement arises without any specific fitting to doping dependent thermal conductivity data.

Using Eq. 2.5 and accounting for porosity, we can calculate the effective thermal conductivity of inverse opals of different shell thicknesses. We assume the grain size to be the same as the shell thickness in these calculations and take the geometric parameter F to be 1 in the boundary scattering rate. Figure 2.4 shows the calculated effective thermal conductivity for inverse opals doped with As at 4×10^{19} cm^{-3}. The overall reduction in thermal conductivity is $\sim 99.6\%$ when compared to bulk silicon.

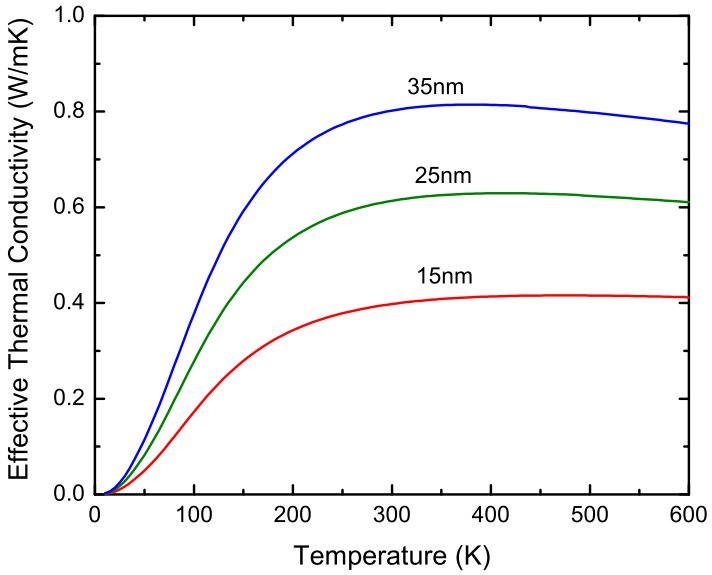

Figure 2.4: The calculated effective thermal conductivity of polysilicon inverse opals as a function of shell thickness. We assume the average grain size to be equal to the shell thickness in these calculations.

2.1.3 Seebeck Coefficient

The Seebeck coefficient, or thermopower, of a semiconductor arises due to carrier diffusion as well as phonon-drag [49]. We discuss each in turn, starting with the diffusion component. Solving Eq. 2.2 in the presence of a temperature gradient yields the contribution due to carrier diffusion. This solution is

$$f_1 = \begin{cases} \tau^* v_x \left(-e\mathcal{E}\dfrac{\partial f_0}{\partial E} + \dfrac{\partial f_0}{\partial x} \right) \left[1 - e^{-z/v_z\tau^*} \right], v_z > 0 \\ \tau^* v_x \left(-e\mathcal{E}\dfrac{\partial f_0}{\partial E} + \dfrac{\partial f_0}{\partial x} \right) \left[1 - e^{(d-z)/v_z\tau^*} \right], v_z < 0 \end{cases} . \tag{2.9}$$

Here $\partial f_0/\partial x$ can be expressed in terms of the temperature gradient as

$$\frac{\partial f_0}{\partial x} = -\frac{\partial f_0}{\partial E}\frac{E - E_F}{T}\nabla_x T. \tag{2.10}$$

Setting J_x (Eq. 2.4) to zero, we obtain the diffusion part of the Seebeck coefficient as

$$\begin{aligned} S_{\mathrm{d}} &= -\frac{\Delta V}{\Delta T} \\ &= -\frac{1}{eT}\left[\frac{\int \Phi(E)\frac{\partial f_0}{\partial E}D(E)E(E-E_f)\tau^* dE}{\int \Phi(E)\frac{\partial f_0}{\partial E}D(E)E\tau^* dE}\right] \end{aligned} \tag{2.11}$$

where the function

$$\begin{aligned} \Phi(E) &= \int_0^d \Bigg\{ \int_0^{\pi/2} \sin^3\theta \left[1 - e^{-z/v_z\tau^*}\right] d\theta \\ &\quad + \int_{\pi/2}^{\pi} \sin^3\theta \left[1 - e^{(d-z)/v_z\tau^*}\right] d\theta \Bigg\} dz \end{aligned} \tag{2.12}$$

arises due to the confinement along the z-direction. The extent to which this extra energy dependence, $\phi(E)$ modifies the Seebeck coefficient from the bulk value depends on the asymmetry of this function with respect to the Fermi energy. Essentially, the function $\phi(E)$ modifies the mean scattering time from τ^* to $\phi(E) \times \tau^*$. When the film thickness is much smaller than the background mean free path, $\phi(E) \times \tau^*$ scales as $E^{-1/2}$, similar to the acoustic phonon relaxation time. At low doping, this has little effect on the Seebeck coefficient, similar to phonon scattering. At high doping, this reduces the Seebeck coefficient by overwhelming ionic impurity scattering. The dominant scattering time scales as $E^{-1/2}$ in inverse opals instead of the usual E^3 dependence in case of dominant impurity scattering. We find the reduction to be quite small in the calculations reported below.

We now turn our attention to the phonon-drag component. This arises due to momentum transfer from phonons to electrons, and thus depends on electron-phonon interactions as well as other phonon relaxation processes. At low temperatures, the drag contributes to most of the thermopower owing to large phonon relaxation times. The contribution reduces significantly at room temperature due to the dominance of Umklapp scattering that reduces phonon mean free paths. Phonon drag has a lesser contribution in low dimensional structures since low frequency phonons that are the main contributors, are randomized by surfaces and grain boundaries. When these interactions are dominant, the phonon drag contribution is effectively zero. Even though we do not expect phonon drag to be a major contributor

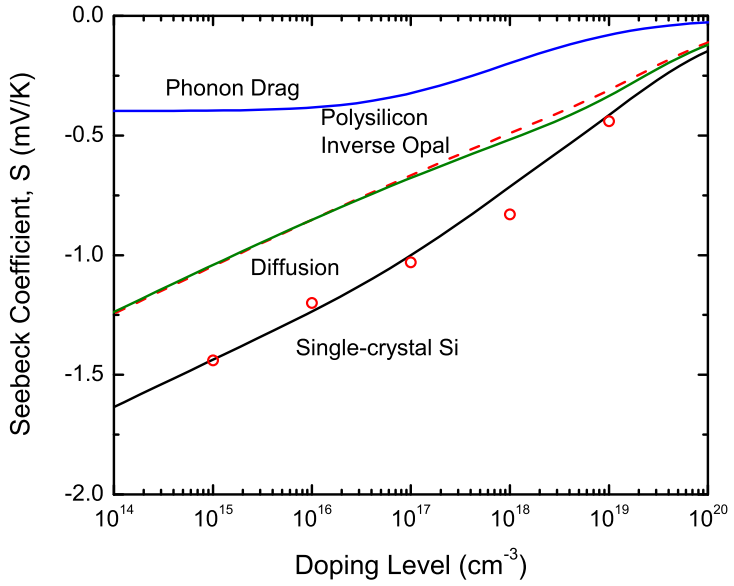

Figure 2.5: The Seebeck coefficient at 300 K as a function of doping. The solid lines represent phonon-drag, carrier diffusion and total Seebeck coefficients respectively in single-crystal bulk silicon. The dashed line is the Seebeck coefficient in polysilicon inverse opals. The open circles are data from Ref. [52].

to the Seebeck coefficient of inverse opals, we include it here for completeness. Wu et al. [50] derived a phonon frequency dependent expression for the phonon drag component using hydrodynamic equations [51] of electron transport. They introduced a non-equilibrium phonon distribution, that models a net momentum transfer between electrons and phonons along a preferred direction. Using their derivation, the phonon drag component is

$$S_{\mathrm{g}} = -\frac{1}{Vne}\sum_{\lambda,\mathbf{q}} \frac{(\hbar w)^2}{k_{\mathrm{B}}T^2}\frac{{q_x}^2}{q^2}\frac{\tau_{\text{e-p}}^{-1}}{\tau_{\text{e-p}}^{-1}+\tau_{\mathrm{p}}^{-1}} n'\left(\frac{\hbar\omega}{k_{\mathrm{B}}T}\right), \tag{2.13}$$

where τ_{p}^{-1} sums all phonon scattering events except phonon-electron interactions and $n'\left(\frac{\hbar\omega}{k_{\mathrm{B}}T}\right)$ is the first derivative of Bose-Einstein distribution with respect to $\frac{\hbar\omega}{k_{\mathrm{B}}T}$. Even though the summation is over all phonon modes, only longitudinal acoustic phonons provide phonon-drag.

In using this model, we first need to fit the deformation potential to the Seebeck data [52]

and find that D_A=1.9 eV fits the Seebeck data for lightly doped single-crystal silicon at 300 K [53, 52] well. We note that this is different from the value that fits both mobility and thermal conductivity data. We suspect that the discrepancy arises due to limitations of the above phonon drag model. The phonon drag component remains constant in bulk silicon until doping exceeds 10^{17} cm^{-3} when it begins to decrease as shown in Figure 2.5. Applying this model to polysilicon inverse opals, we find that the phonon-drag component is negligible. The Seebeck coefficient arises almost entirely due to carrier diffusion. There is a small difference between the diffusion component in polysilicon inverse opals and bulk silicon, at doping levels above 10^{17} cm^{-3} due to differences in the dominances of scattering mechanisms. Surface and grain boundary scattering dominates in inverse opals while ionic impurity scattering dominates in bulk silicon, leading to slight differences in the Seebeck coefficient, as discussed previously.

2.2 Results and Discussion

In this section, we combine the thermoelectric properties from the previous section to further investigate thermoelectric energy conversion in inverse opals. Figure 2.6 plots the power factor of polysilicon inverse opals with shell thickness 25 nm. We assume that the structure has been sufficiently annealed such that the grain size is comparable to the shell thickness. We plot the power factors for bulk silicon, a single-crystal 25 nm thick silicon film and bulk polysilicon respectively for comparison. The power factor peaks at 4×10^{19} cm^{-3} in all cases which is a property of the band structure, and is unaffected by shell thickness or grain boundaries. The plateau in the curve for bulk silicon after $\sim 10^{18}$ cm^{-3} arises due to decrease in the phonon drag component of the Seebeck coefficient. This vanishes in all other structures due to an overall reduction in the phonon drag component. Reduction in electrical conductivity reduces the peak power factor by $\sim$94% in the inverse opal.

The reduction in power factor is effectively countered by a more dramatic reduction in thermal conductivity. Figure 2.7 plots the ratio of electrical to thermal conductivities in comparison to the ratio in bulk single-crystal silicon as a function of varying feature sizes. The grain size is set equal to the shell thickness in all calculations. At a feature size of 25 nm,

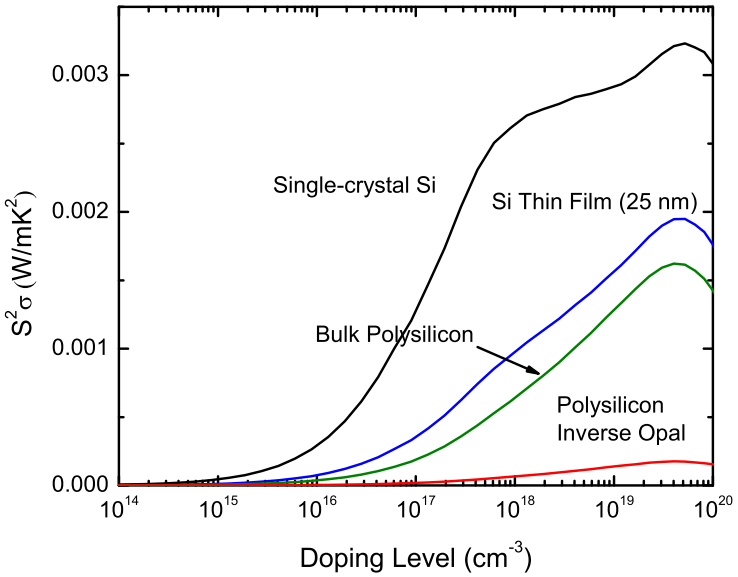

Figure 2.6: The power factor for different silicon structures at 300 K as a function of doping.

boundary scattering in thin films increases this ratio by an order of magnitude compared to bulk silicon. Grain boundaries are slightly better than crystal surfaces in providing such enhancement. In bulk polysilicon, the enhancement is approximately fourteen times compared to bulk single-crystal silicon. The inverse opal geometry combines both surface and grain boundary scattering and provides an enhancement of $\sim$18 compared to bulk silicon.

A surprising result in the above figure is that grain boundary scattering is better than surface scattering in enhancing the figure of merit in inverse opals. Exploring this further, Figure 2.8 compares the energy dependent mean free paths for electrons and phonons at a grain size of 25 nm. We use the scattering rates described in Eq. 2.1 and Eq. 2.6. The figure also shows the energy independent Casimir limit [54] for mean free path from boundary scattering. Grain boundary scattering reduces the mean free paths of electrons and phonons similarly up to energies of $\sim$0.01 eV (2.4 THz). At higher energies, the electronic mean free path saturates at $\sim$13 nm while the phonon mean free path continues to decrease sharply. Since the transport of electrons with energy $\lesssim$0.01 eV is limited by ionic impurity scattering rather than grain boundary scattering, grain boundaries do not affect charge

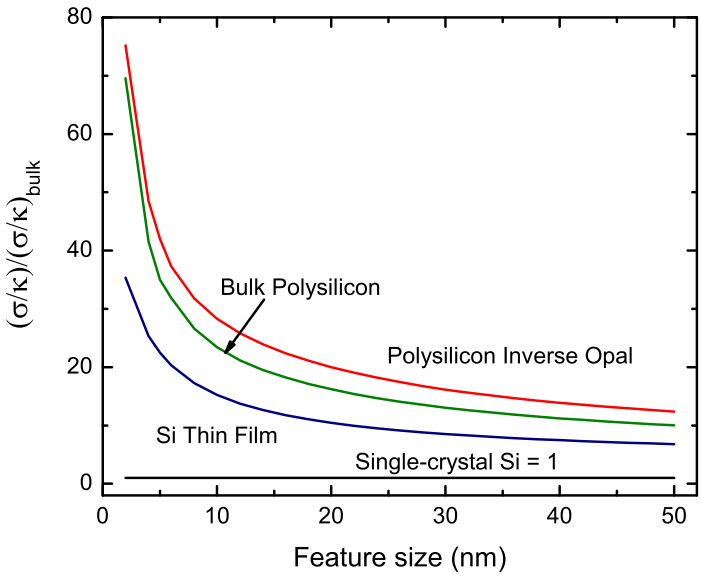

Figure 2.7: The ratio between the electrical and thermal conductivities in relation to the ratio for bulk silicon. The doping level is 4×10^{19} cm^{-3} and the temperature is 300 K for all curves. Grain boundaries contribute more to the enhancement than surfaces as evident from the curves for thin film and polycrystalline silicon with similar feature size. Inverse opals combine both effects and are slightly better than bulk polysilicon when the grain size equals the shell thickness.

transport significantly in the range of feature sizes considered here. The impact on heat conduction is, however more dramatic since the mean free path of room temperature phonons is reduced well below the Casimir limit.

Referring again to Figure 2.7, the larger surface area in an inverse opal does not provide a dramatic increase compared to bulk polysilicon when the grain size in the inverse opal equals the shell thickness. However, unlike bulk polysilicon, the grain size in an inverse opal is limited by the shell thickness which provides an opportunity to further reduce the grain size for optimal ZT. We explore this below in our discussion on the figure of merit. The enhancement factor for inverse opals increases to $\sim$28 as the shell thickness and grain size decrease to 10 nm. In contrast, the enhancement using a 10 nm thin film is only a half of this. It is clear that theoretically, grain boundary scattering has a greater impact on the figure of merit than boundary scattering. We have discussed the reason for this above. We

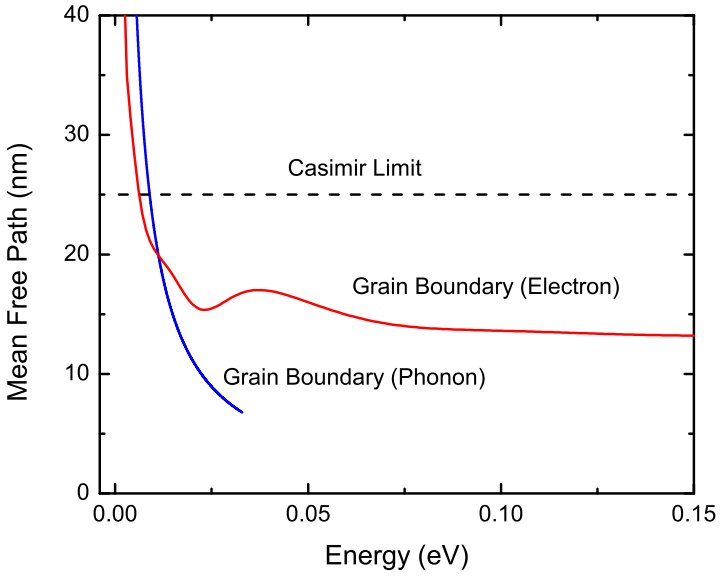

Figure 2.8: The mean free path of electrons and phonons due to grain boundary scattering as a function of energy. Mean free paths for electrons are consistently larger than those for phonons expect at very low energies that do not contribute significantly to conduction. The Casimir limit is shown for comparison with boundary scattering.

explore the relative magnitudes in the context of inverse opals next.

Figure 2.9 shows the figure of merit at 300 K and 600 K for polysilicon inverse opals based on the above calculations. We include the electronic contribution to the thermal conductivity here using the Wiedemann-Franz law. This results in a modest increase in the thermal conductivity by $\sim$ 5 % at 300 K. The ratio, r is the ratio between the average grain size and the shell thickness. In typical inverse opals, the shell thickness is $\gtrsim$15 nm. The upper bound on grain size is the shell thickness[55], corresponding to r=1. For the lower limit, we consider grains $\gtrsim$5 nm, to avoid quantum confinement effects[56] that would reduce the free carrier concentration. This corresponds to r=1/3 for a shell thickness of 15 nm.

For shell thicknesses in the range 20–50 nm, the figure of merit increases by $\sim$50 % at 300 K when the average grain size is a third of the shell thickness. At 10 nm shell thickness, maintaining the grain size at a third of the shell thickness results in a $\sim$25 % increase in ZT. For shell thicknesses in the range 10–25 nm, the figure of merit ranges between 0.12–0.15 at

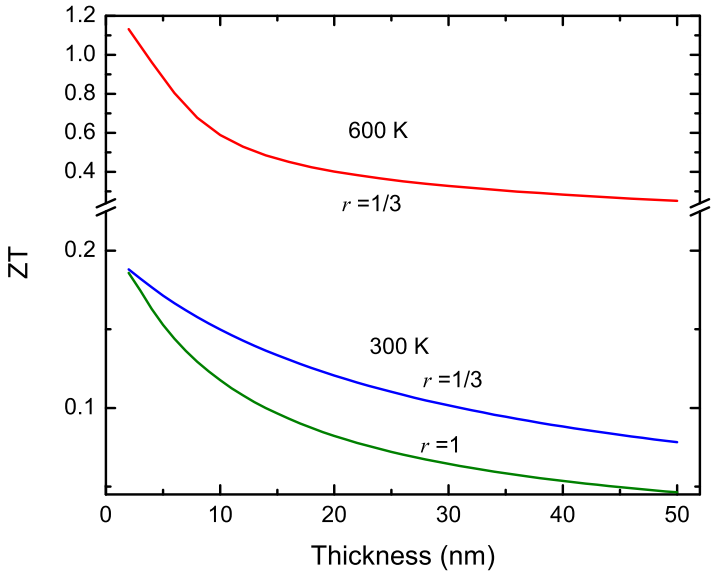

Figure 2.9: The projected ZT as a function of shell thickness. The solid curves represent different ratios, r of the average grain size to the shell thickness. Choosing grain sizes smaller than the shell thickness enhances the figure of merit for feature sizes $\gtrsim$10 nm.

300 K when r=1/3. The same range of features provides a range of 0.36–0.60 in ZT at 600 K. Thus, the impact of decreasing feature size is not significant at room temperature but is substantial at elevated temperatures.

These calculations show that inverse opals with features $\lesssim$25 nm that maintain a grain size smaller than the shell thickness provide a significant enhancement in the figure of merit and are comparable to single-crystal silicon nanowires. Overall, the figure of merit remains inferior when compared to data from single wires [6]. However, any practical implementation using nanowires requires an array of wires with substantial variations in properties and inferior electrical contact resistances [57] when compared to inverse opals [58, 59]. It is difficult to claim that the non-idealized conversion efficiency will necessarily be superior for nanowires. There remain substantial practical challenges with inverse opals as well. Doping is a key practical issue [59]. In-situ doping [38, 60] during film deposition followed by annealing and activation at relatively low temperatures is needed to prevent grain growth significantly [61]. This should form the emphasis of future experimental work in this area.

2.3 Conclusion

In summary, we present a model for thermoelectric properties of highly doped polysilicon inverse opals. Nanoscale grains in addition to the large surface area available for scattering phonons result in a net enhancement in the figure of merit for thermoelectric energy conversion. A surprising result is that a smaller grain size yields a larger ZT. We understand this in terms of the relative impact of nanoscale grains on electron versus phonon transport. We find that ZT exceeds 0.1 at room temperature and can be as high as 0.6 at 600 K. Future experimental work should investigate the fabrication of inverse opals with small grain sizes as well as the possibility of doping the structures in-situ followed by low temperature annealing to preserve grain size. This work provides theoretical understanding of charge and heat transport in nanostructured inverse opals, and suggests directions for future experiments on the thermoelectric properties of these materials.

CHAPTER 3

EXPERIMENTS AND RESULTS

In this chapter, I will mainly discuss the thermal conductivity measurement and present the results up to date. We measure the thermal conductivity of polysilicon inverse opal using the 3ω method. The measurement went down to as low as 15 K. Various characterization techniques were involved in this measurement. We use transmission electron microscopy and X-ray diffraction to characterize the grain size. Finally, an empirical model for thermal conductivity of inverse opal structure is provided based on the results.

3.1 Sample Fabrication

The silica colloids were made using the well-known Stober method [62] and the opals were assembled by vertical deposition [63] as shown in Figure 3.1a. We can vary the thickness of the opal structure (i.e. number of layers) either by increasing the solid content of the silica spheres in the solvent (which is ethanol in our case) or the temperature of the incubator. We usually grow the opal for overnight in the incubator at 35–37 °C. The opal structure is shown in Figure 3.1b and c. Due to the nature of the vertical deposition method, the number of layers increases from one edge and reaches a constant for the rest of the sample. Under these conditions, we usually get 5–10 layers of sillica colloids. After that we deposit amorphous silicon on the opal structure by chemical vapor deposition (CVD) at 325 °C for 5 hours under pressure $\sim 10^{-6}$ mbar. The pores in the opal structure is filled to its maxima.

We then annealed the sample at 1000 °C for 10 hours in the tube furnace under forming gas to recrystallize the amorphous silicon. The temperature ramping rate is 10 °C per minute. The silica opals were then removed with an ethanol solution of hydrofluoric acid (5%). The sample was left in the solution for 20–25 minutes, rinsed gently with ethanol and dried in

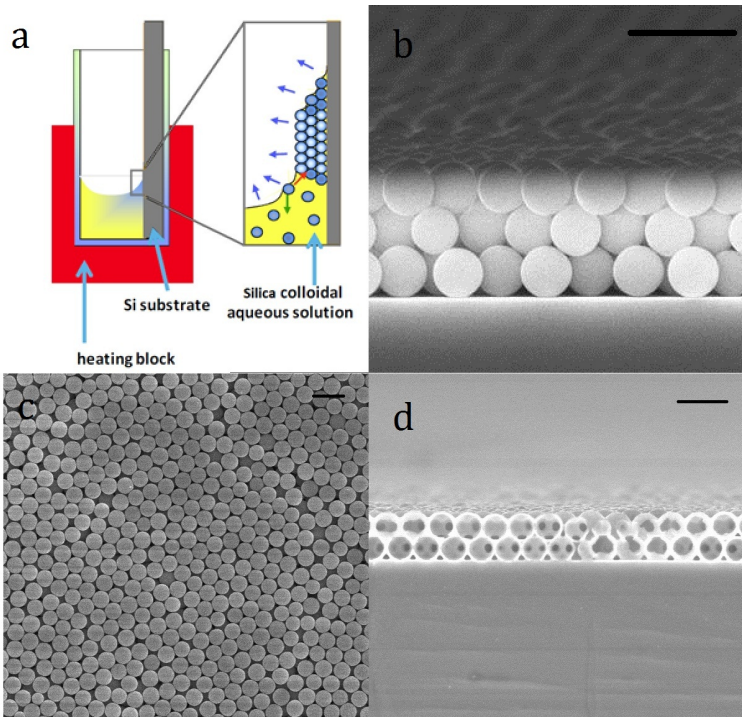

Figure 3.1: a. Opal assembly schematic. SEM of opal structure before CVD: b. side view, c. top view; d. Silicon inverse opal. The scale bar is 1 μm in all SEMs.

the hood. The inverse opal structure is shown in Figure 3.1d.

3.2 Thermal Conductivity Measurements

3.2.1 The 3ω Method

Any measurement on thermal conductivity requires two quantities: the heat flow and the temperature gradient. The 3ω method [20, 64] is a frequency domain method that uses a resistive metal line (in most cases) to both act as a heater and a thermometer. The good accuracy in heat flow and temperature change makes this method very powerful in measuring thermal conductivity of thin films. A 3ω device usually consists of a bulk substrate, a thin film of interest and a heater (thermometer) as shown in Figure 3.2. If the thin film is electrically conductive, a dielectric layer is required to prevent any electrical leakage from the heater. In this measurement, we deposit ~100 nm silicon dioxide to ensure good electrical

insulation. The metal heater is fabricated using gold evaporation through a shadow mask.

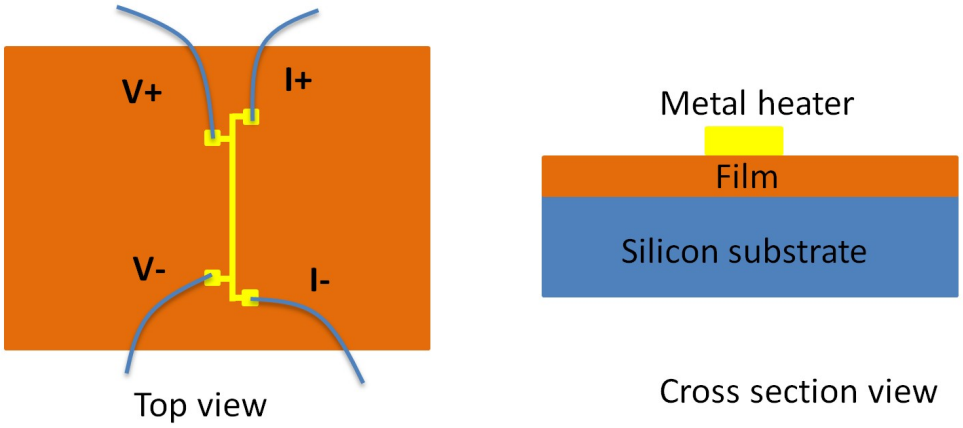

Figure 3.2: The schematic of a 3ω device.

When an AC current of frequency ω is supplied by a current (or voltage) source, the heater generates a heat flow that has a DC component and an AC component oscillating at 2ω. The AC heating produces a temperature fluctuation at the same frequency, $\Delta T_{2\omega}$. Since the resistance of the heater is temperature dependent, the temperature fluctuation brings a resistance change, which is also oscillating at 2ω. The 1ω current and the 2ω resistance change generate a 3ω voltage $V_{3\omega}$, through which, $\Delta T_{2\omega}$ can be extracted, hence the thermal property of the sample. The relationship between $\Delta T_{2\omega}$ and $V_{3\omega}$ is given by [20]

$$\Delta T_{2\omega} = 2\frac{V_{3\omega}}{V_0} R_0 \left(\frac{dR}{dT}\right)^{-1}, \tag{3.1}$$

where R_0 is the average resistance of the heater, V_0 the 1ω voltage across the heater and $V_{3\omega}$ is the 3ω voltage generated in the heater. dR/dT is the temperature coefficient of the heater resistance, which is obtained by differentiating the heater calibration curve (resistance as a function of temperature).

The schematic circuit diagram is shown in Figure 3.3. We use a lock-in amplifier (SR830) to detect the voltage at 3ω. Since SR830 has a high dynamic reserve (>100dB) and is able to pick up the 3ω voltage from the large background 1ω signal [64], we did not use any noise cancelation scheme, such as nulling a bridge [65]. We use the built-in voltage generator in

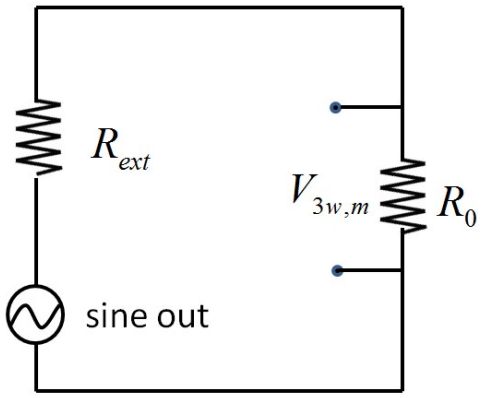

Figure 3.3: The schematic circuit diagram of the experiment set up.

the lock-in to supplier the current to the heater. While this practice simplifies the whole set up, it creates a small issue: the measured 3ω voltage, $V_{3\omega,m}$ is not the one generated by the heater, $V_{3\omega}$, as a voltage source has a small internal resistance that is comparable to the heater resistance. To convert the measured value to the generated value, we use the following relation:

$$V_{3\omega} = \frac{R_{ext} + R_0}{R_{ext}} V_{3\omega,m}, \tag{3.2}$$

where R_{ext} is the total resistance in the circuit except the heater. Note that in the case of a current source (sufficiently large R_{ext}), $V_{3\omega}$ is equal to $V_{3\omega,m}$.

3.2.2 Data Reduction

The temperature oscillation in Eq. 3.1 has the information of the thermal properties of the material underneath. By employing a thermal model and fitting the experimental data, the thermal conductivity of the thin film can be deduced.

In the case that the thermal penetration depth $L = \sqrt{(\alpha/2\omega)}$ is much larger than the thin film thickness t and the heater width $2b$, but still smaller than the substrate thickness, and $2b$ is large compared to t, the heat equation has a simpler form [20]:

$$\Delta T = \frac{P}{\pi L \kappa_s}\left(0.5\ln\left(\frac{\alpha_s}{b^2}\right) - 0.5\ln(2\omega) + 0.923 - i\frac{\pi}{4}\right) + \frac{Pt}{2bL\kappa_f}. \tag{3.3}$$

Here, P is the Joule heating power, L the heater width, κ and α are the thermal conductivity and diffusivity, and the subscript s, f are for substrate and film. Note that in Eq. 3.3, the first part on the right hand side is the temperature fluctuation in the substrate ΔT_s and the second part is that in the film ΔT_f. The thermal conductivity of substrate and film can be determined separately as follows:

$$\kappa_s = -\frac{P}{2\pi L}\left(\frac{d\Delta T}{d\ln(2\omega)}\right)^{-1}; \tag{3.4}$$

with the knowledge of κ_s, ΔT_s can be obtained, hence ΔT_f; and then

$$\kappa_f = \frac{Pt}{2bL\Delta T_f}. \tag{3.5}$$

However, the conditions above cannot always be satisfied, especially when the measurement covers a wide range of temperatures. Borca-Tascuic [66] has worked out the analytical solution to the N-layer system. In the case that the in-plane and out-of-plane thermal conductivity are the same, the solution has the following form:

$$\Delta T = \frac{-P}{\pi l \kappa_1}\int_0^\infty \frac{1}{A_1 B_1}\frac{\sin^2(b\lambda)}{b^2\lambda^2}d\lambda, \tag{3.6}$$

where

$$\begin{aligned} A_{i-1} &= \frac{A_i\frac{\kappa_i B_i}{\kappa_{i-1}B_{i-1}} - \tanh(\phi_{i-1})}{1 - A_i\frac{\kappa_i B_i}{\kappa_{i-1}B_{i-1}}\tanh(\phi_{i-1})}, i = N...2 \\ B_i &= \left(\lambda^2 + \frac{i2\omega}{\alpha_i}\right)^{1/2}, \phi_i = B_i d_i. \end{aligned}$$

Here, λ is the integration variable, the subscript i denotes ith layer from the top and d is the thickness of each layer. The value of A_n depends on the boundary condition (BC) of the substrate (nth layer from the top). A_n is equal to $-\tanh(\phi_n)$ for adiabatic BC, and $-1/\tanh(\phi_n)$ for isothermal BC.

In our measurement, we use the full solution to the heat equations. The silicon inverse opal layer is treated as a thin film on the substrate. Therefore, the thermal conductivity

obtained from the fitting calculation is the effective thermal conductivity of the film. The material conductivity is determined using the relationship[15] discussed in Chapter 1.

3.2.3 Experiment Details

The gold thermometer is calibrated in a cryostat to obtain the temperature coefficient dR/dT. A helium dewar is connected to the cryostat using a transfer line and the cryostat is controlled by a Lake Shore temperature controller. We use a lock-in amplifier to send an AC current of ∼250 nA to the metal line and measure the voltage drop. Our measurement went well below 50 K where the resistance temperature relationship is no longer linear. I use the Bloch-Gruneisen Formula [67] to fit the calibration data and differentiate the analytical curve at each temperature point to get dR/dT. The Bloch-Gruneisen Formula is

$$\rho(T) = \rho(0) + A\left(\frac{T}{T_D}\right)^n \int_0^{T_D/T} \frac{x^n}{(e^x - 1)(1 - e^{-x})} dx, \tag{3.7}$$

where x is the integration variable, $\rho(0)$ is the residual resistivity due to defect scattering, A is a constant that depends on the velocity of electrons at the Fermi surface, the Debye radius and the number density of electrons in the metal. n is equal to 5 for simple metals. T_D is the Debye temperature. This formula fits our calibration data very well as shown in Figure 3.4. I found that for each heater, T_D is always slightly smaller than the Debye temperature obtained from specific heat measurements.

As the temperature is reduced well below the Debye temperature, fewer phonon modes become active. As a result, the resistivity usually drops the linear-like relationship with temperature and finally reaches a constant value, known as the residual resistivity. This value depends not only on the type of metal, but on its purity and thermal history. We found that when the temperature is below 10 K, the resistance of the gold heater becomes insensitive to temperature. Therefore, it is no longer capable of being a thermometer. The data below 10 K is not included in the final thermal conductivity results. The temperature coefficient, dR/dT, is shown in Figure 3.5 for one heater.

The first two points are very close to zero. As temperature increases, the coefficient dR/dT

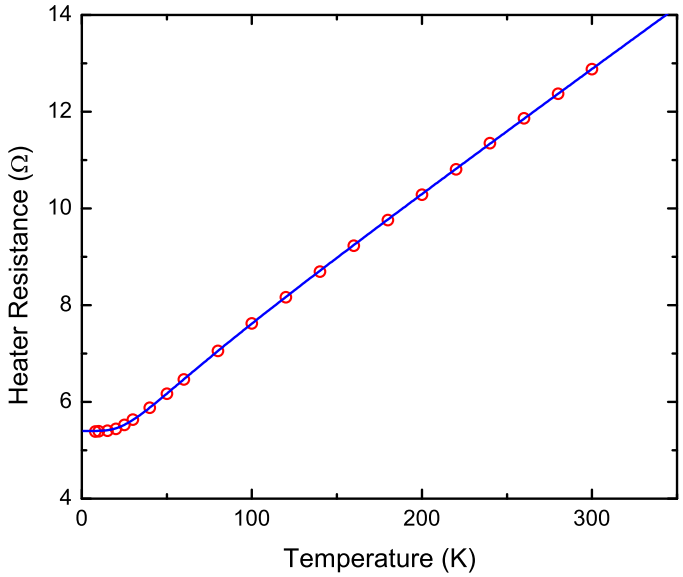

Figure 3.4: The heater resistance calibration (open circles) and the Bloch-Gruneisen Formula fitting (solid line).

keeps increasing until 50 K, where it reaches its maxima. It then decreases gradually. The temperature coefficient is almost constant above the Debye temperature (170 K for gold). All the gold heaters exhibit similar trend.

Our ultimate goal is to obtain the thermal conductivity of the inverse opal layer by fitting the temperature oscillation with the heat equations, i.e. Eq. 3.6. Therefore, we need to know other parameters as accurate as possible to reduce the uncertainty in thermal conductivity. The heater geometry is easily obtained from SEM images. The thickness of the silicon dioxide layer is characterized on a dummy sample using ellipsometry. However, since the opals were assembled by vertical deposition [63], the number of opal layers varies along one direction. As a result, it is difficult to get the exact thickness of the inverse opal layer underneath the heater. The layer thickness is a critical parameter and affects the resultant thermal conductivity directly. In order to address this issue we use focused ion beam (FIB) to cut an opening close to the heater and image the cross section at a tilted angle as shown in Figure 3.6. The thickness is then obtained from the projected cross section. As the heater sits on the top surface that is not perfectly flat, the thickness has an uncertainty that is

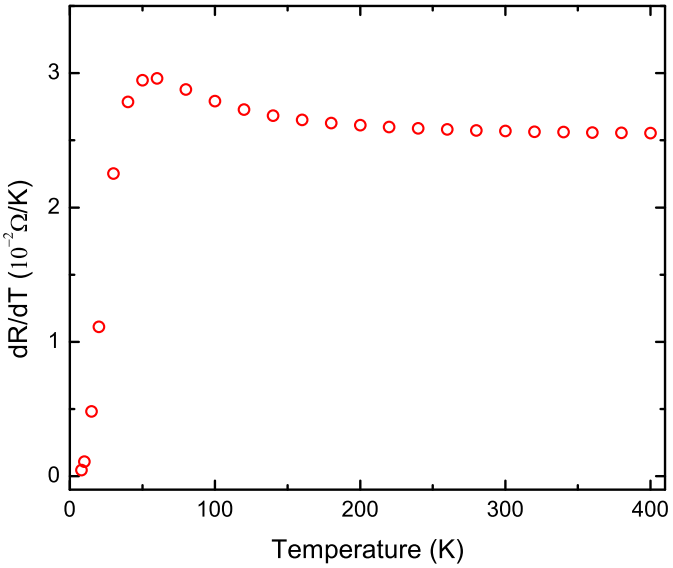

Figure 3.5: The heater temperature coefficient plotted vs. temperature. The data below 10 K is abandoned.

comparable to the silica radius. The percentage uncertainty is smaller with multiple opal layers.

3.2.4 Results

We use LabVIEW to control the instruments and take data from the lock-in amplifier. Using Eq. 3.1 and 3.2, we know the temperature oscillation ΔT from the measured third harmonic voltage, $V_{3\omega,m}$ at each frequency. Since all the geometric parameters have been determined, the only unknowns are the thermal properties of the inverse opal layer and substrate (we use bulk properties of silicon dioxide). As discussed in previous sections, the thermal conductivities of substrate and inverse opal layer can be determined separately from the linear region. Figure 3.7 shows the temperature oscillation at 15 K normalized by power and the fitting curve. Both in-phase and out-of-phase data are presented.

In the actual measurement, we found that the silicon dioxide contribution to the total temperature oscillation is negligible. So is the contact resistance between heater and silicon

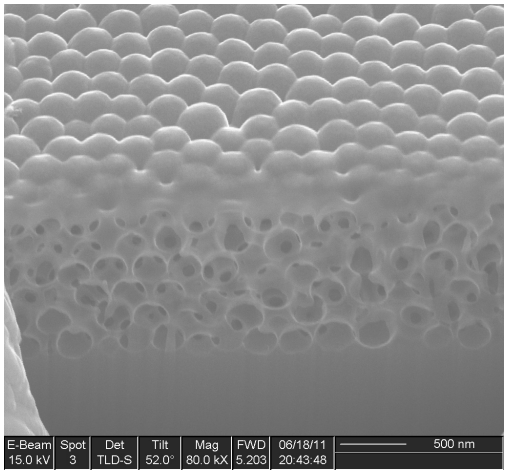

Figure 3.6: The cross section of the inverse opal layer. The opening was cut by FIB.

dioxide. This is due to the large thickness ($\sim$5 μm) and small effective thermal conductivity of the inverse opal layer, hence a large thermal resistance. As a result, most of the temperature drop occurs in the inverse opal layer. The in-phase component is almost flat in the low frequency region, indicating that the substrate thermal conductivity is very high, which is indeed the case at low temperature. However, again, the temperature oscillation is insensitive to the substrate, so the substrate thermal conductivity determined in this way would have a relatively big uncertainty.

Theoretically, one can determine the heat capacity from the "tail" in the high frequency region, where the thermal penetration depth is comparable to the inverse opal layer thickness. However, we found that this method will only give us a rough value of the heat capacity. The uncertainty is much larger than that in the thermal conductivity measurement.

By doing the fitting at each temperature, we get the temperature trend of thermal conductivity. We have measured three samples with different shell thicknesses in total. The diameters of silica spheres are 635 nm, 420 nm and 300 nm, and the corresponding shell thicknesses are $\sim$38 nm, 25 nm and 18 nm. Figure 3.8 shows the complete experimental results in this study up to date. The right axis represents the effective thermal conductivity of the inverse opal layer. This is obtained from fitting the temperature oscillation with the heat equations. The effective thermal conductivities for all three samples are below 2 W/mK at 300K. This is no surprising because firstly the inverse opal layer is a extremely porous struc-

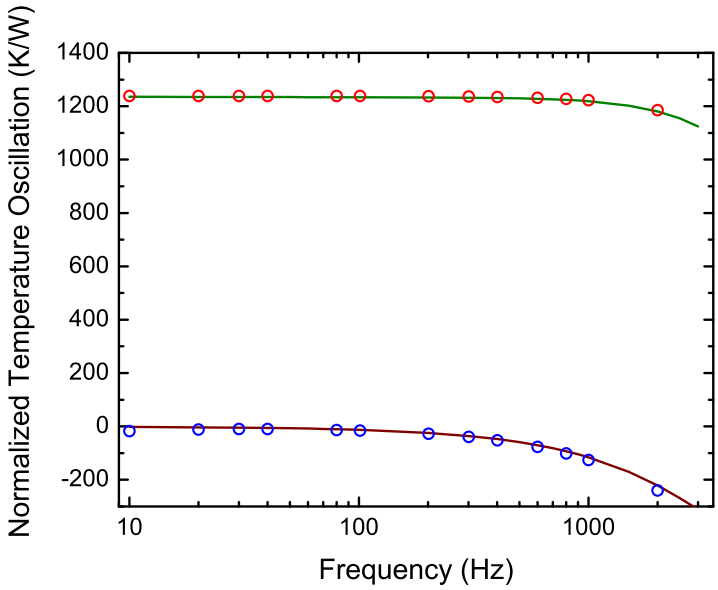

Figure 3.7: Normalized temperature oscillation data (open circles) and fitting curve (solid curves).

ture (78% porosity), secondly the small shell thickness and noncrystalline material enhances phonon scattering.

The left axis is for the material thermal conductivity. The relationship between effective and material thermal conductivity has been discussed in Chapter 1. As we fill the pores in the opal assembly to its maxima, the ratio between effective and intrinsic material conductivity is ∼0.115. The material conductivity allows us to investigate the phonon transport in such small dimension polycrystalline structure. Comparing this figure with Figure 2.4 in Chapter 2, the trend at high temperature agrees with each other quite well. However, they don't have a good match at low temperatures. The reasons and possible modifications will be discussed in later sections.

From the three different curves, there is a clear correlation between thermal conductivity and shell thickness as expected. The larger the thickness is, the larger the thermal conductivity. While phonon-surface and phonon-grain boundary scattering are dominant in all three samples, Umklapp scattering is also very important in the large shell thickness sample, as the thermal conductivity decreases at high temperature.

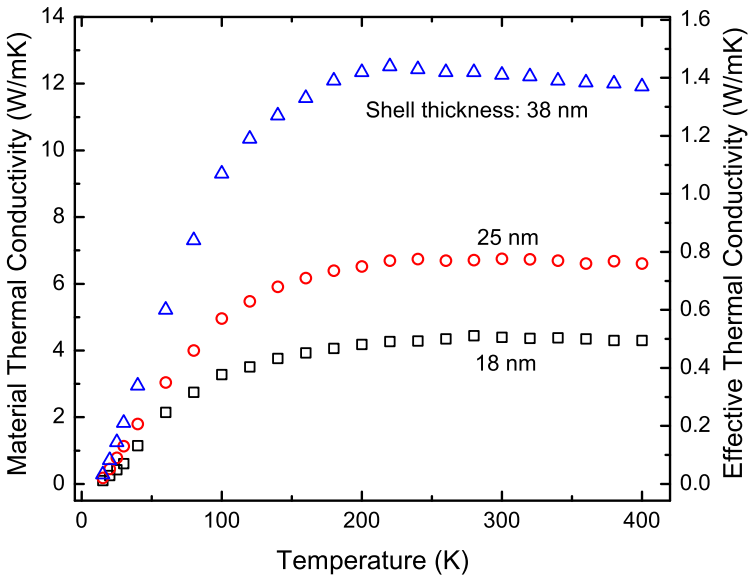

Figure 3.8: Measured thermal conductivity of the inverse opal structure for different silica sizes (or shell thickness). The left axis is for material thermal conductivity while the right is for effective thermal conductivity of the layer.

3.3 Grain Size Characterization

As discussed in Chapter 2, grain boundary has a bigger impact on the thermal conductivity than surface boundary. It is impossible to interpret the thermal conductivity results without knowing the grain size. It has been found that the grains in recrystallized polycrystalline material has a log-normal distribution [28, 42]. Also, the grain size of a thin film polycrystalline material is limited by the film thickness [55]. Therefore, given that the samples were annealed at 1000 °C for 10 hours, we expect the grains in silicon inverse opal to have a log-normal size distribution with average grain size similar to shell thickness.

A common way to characterize the grain size and its distribution is to use scanning electron microscopy (SEM). SEM is able to image a large region that has hundreds of grains. However, the lower limit for SEM is ∼50 nm, and our sample has much smaller grain size. The only way to distinguish the atomic orientation is to use transmission electron microscopy (TEM). Figure 3.11 shows the TEM image of an inverse opal with inner diameter of 300 nm. The

shell thickness from the left image is larger because the breakage did not happen along the diameter. The polycrystalline nature of the material is confirmed from image on the right. The yellow dashed lines indicate grain boundaries. The grain size is indeed comparable to shell thickness.

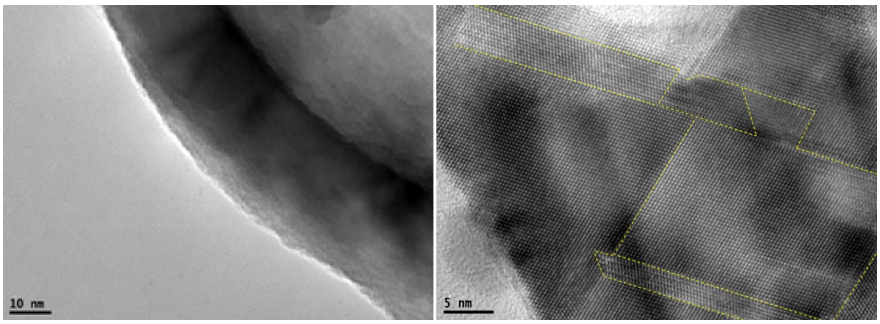

Figure 3.9: TEM of silicon inverse opal structure. The scale bars are 10 nm and 5 nm respectively.

However, the region that a TEM image can cover is very limited. We often end up with only several grains in one image. Given such small number of grains, we cannot extract the size distribution. The average grain size will also have a large error. Therefore, we turned to X-ray diffraction (XRD).

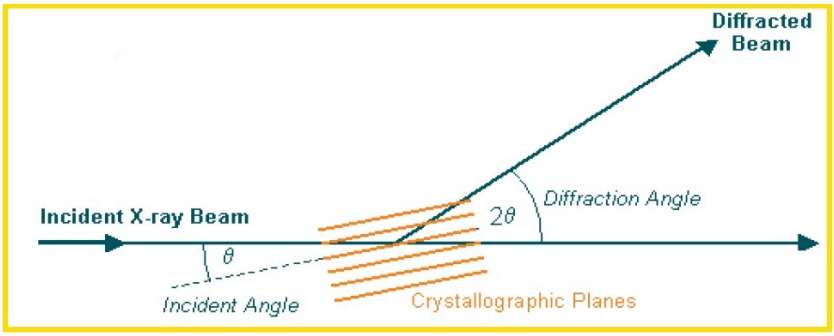

Figure 3.10: The schematic diagram of the XRD method.

XRD is a non-destructive method which reveals information about the crystal structure. During the measurement, a beam of X-rays strikes a crystal and causes the beam of light to spread into many specific directions. From the angles and intensities of these diffracted beams, the crystal structure of the sample can be determined. In our case, the polysilicon

inverse opal is on a single crystal silicon substrate, so the diffracted beam will have the information of both single crystal silicon and polysilicon. However, the peaks are located at different angles. From the shape of the polysilicon peaks, we can extract the average grain size. The XRD method is easier and quicker than TEM. However, it cannot reveal the size distribution of grains.

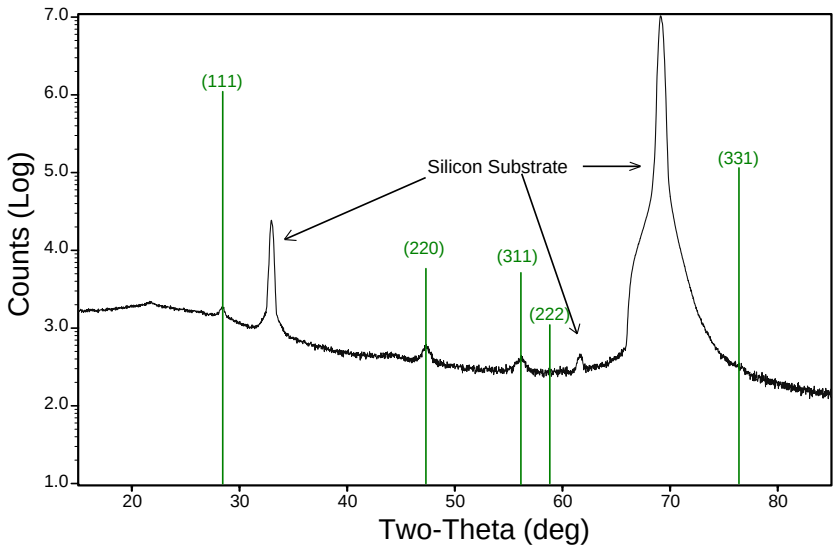

Figure 3.11: Intensity counts from a typical XRD analysis. The peaks with vertical green lines are from polysilicon inverse opal.

We use the Jade software to analyze the XRD data. The software analyzes each peak and gives the average grain size for that atomic orientation. The average grain size for all the atomic orientations is carried out by a weighted average based on the uncertainty in each orientation. The average grain sizes for all three samples are listed in Table 3.1, with silica diameter and shell thickness.

3.4 Discussion

We used the dispersion proposed by Holland [40] to calculate the thermal conductivity of polysilicon inverse opal in Chapter 2. Now given the measured data, it is time to examine

Table 3.1: Feature Size of Different Samples

Sample #	Silica Diameter	Shell Thickness	Avg. Grain Size (uncertainty)
1	635 nm	38 nm	44(16) nm
2	420 nm	25 nm	24(4) nm
3	300 nm	18 nm	20(2) nm

the validity of the model. Again, we use Eq. 2.5 and the expressions of different scattering rates in Chapter 2. The constants in the scattering rates are also the same. We plug in the shell thickness and average grain size from Table 3.1. By changing α in Eq. 2.6, we try to match the measured data. However, the fitting is not good as apparent in Figure 3.12.

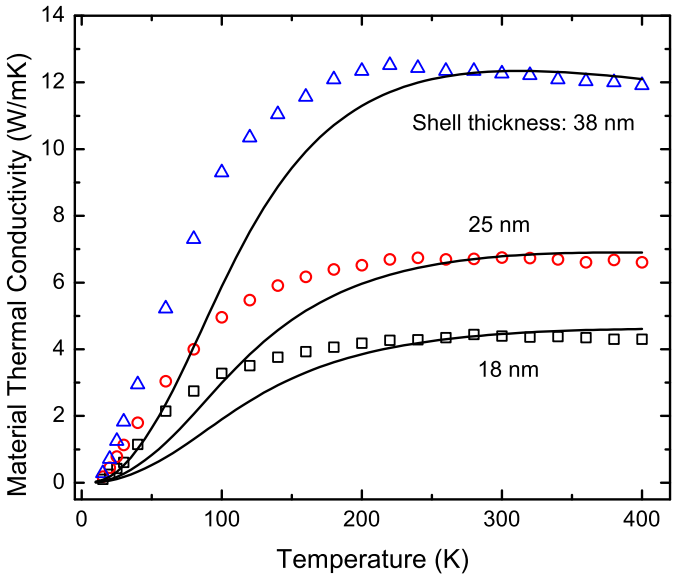

Figure 3.12: Comparison of the thermal conductivity data of polysilicon inverse opal with Holland's model.

The model consistently underestimates the thermal conductivity at low temperature. If we want to match the low temperature data by increasing α, the high temperature data will be way off. The reason for this discrepancy is the phonon dispersion we use, which overestimates the speed of high energy phonons. Even though Holland used a cut-off frequency lower than Debye frequency for LA branch, the phonon propagation speed is still too high near the zone boundary. These low-speed high-energy phonons contribute a significant portion to

heat capacity, but a lot less to thermal conductivity. In order to address this issue, we can calculate the real dispersion relation using lattice dynamics with spherical shells as boundary conditions. However, this is out of the scope of this study. Instead, we adopt Holland's dispersion with a lower cut-off frequency for LA phonons, $\omega_{c,LA}$. Due to the dominant Umklapp scattering in bulk silicon, the selection of $\omega_{c,LA}$ is not as important. However, this cut-off frequency is particularly important for small dimension structures. We iteratively determine $\omega_{c,LA}$ as follows. First we adjust $\omega_{c,LA}$ to fit the thermal conductivity data of sample 1 (38 nm shell thickness). Second, using the new $\omega_{c,LA}$ we adjust the constants in Umklapp scattering, B and C to fit the bulk data. Then we adjust $\omega_{c,LA}$ again with new values of B and C. The iteration is continued until $\omega_{c,LA}$, B and C match data of both bulk silicon and sample 1 reasonably well. The final values of $\omega_{c,LA}$, B and C are 5.1×10^{13} rad/s, 1.7×10^{19} s/K and 150 K, respectively.

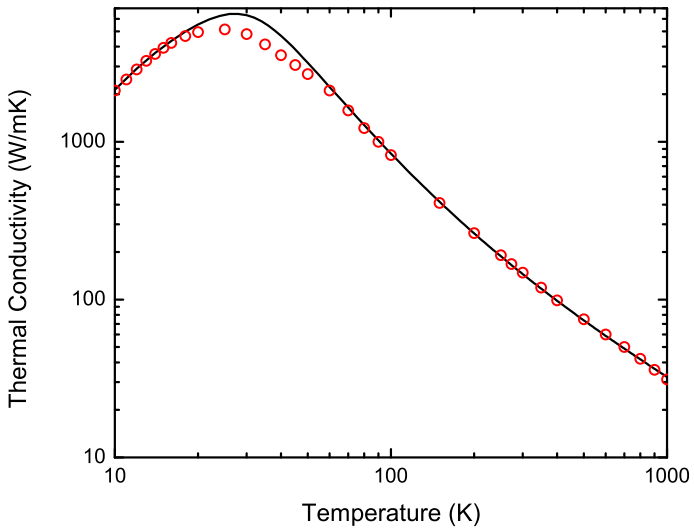

Figure 3.13: Comparison of the bulk thermal conductivity data with Holland's model (with lower cut-off frequency).

Figure 3.13 shows the theoretical calculation of bulk silicon and the reported values [40] from 10 K to 1000 K. The calculation matches the experimental data fairly well except for some deviations between 10–50K, where impurity scattering is important in bulk silicon.

Now let's turn to the case of polysilicon inverse opal. We use the same procedure as producing Figure 3.12, except that the cut-off frequency for LA branch is 5.1×10^{13} rad/s. By treating α in Eq. 2.6 as the only fitting parameter, we can fit the measured data fairly well. However, the shape factor F in surface scattering is not accurate. The exact value is not known at this point given the complex shape, but a quick guess gives a factor large than 1 as the surface to volume ration is smaller than nanowires. If we take $F = 2$, the fitting is slightly better. The result is shown in Figure 3.14. The fitting parameter α is 1, 0.85 and 0.65 for sample 1, 2 and 3, respectively.

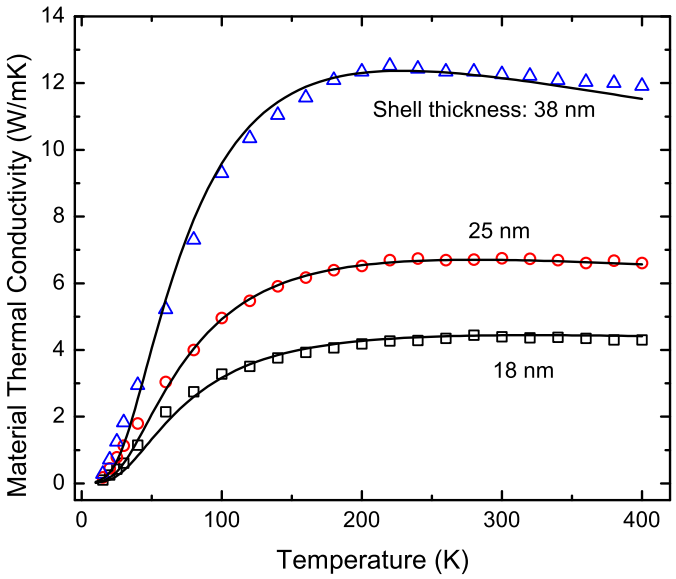

Figure 3.14: Comparison of the thermal conductivity data of polysilicon inverse opal with Holland's model (with lower cut-off frequency).

Comparing Figure 3.14 with Figure 3.12, it is obvious that this model with a lower cut-off frequency is much better than Holland's model in predicting the thermal conductivity of polysilicon inverse opal. However, the physics at low temperature is still unclear. While we adopt the scattering rates for surface and grain boundary scattering from literature, there is still an interplay between these two interactions. If I plot only the low temperature part in a log-log scale, the thermal conductivity trend is more towards T^2 as in Figure3.15.

This trend is unlike the T^3 trend found in single crystal bulk silicon [40], large nanowires [68],

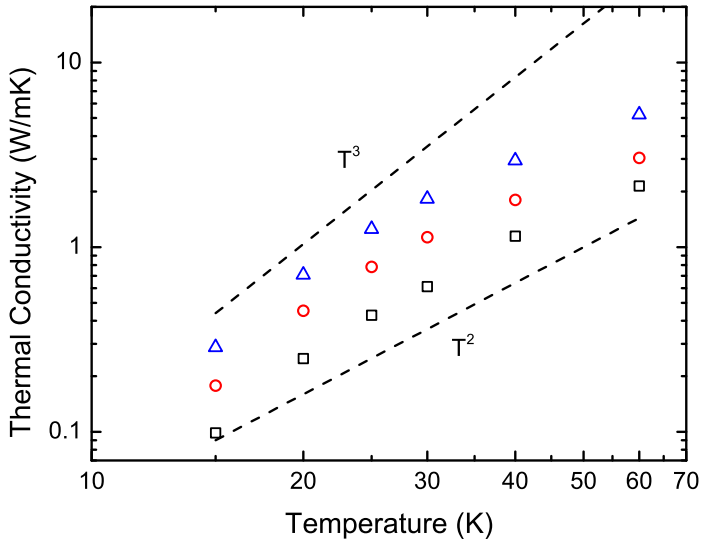

Figure 3.15: Thermal conductivity data of polysilicon inverse opal at low temperature.

but similar to polysilicon [42]. The T^3 trend in thermal conductivity comes from the T^3 relation in heat capacity and a frequency independent phonon mean free path at low temperature. In our case, T^2 trend implies that the mean free path is frequency dependent. We have used Eq. 2.6 which gives a mean free path inversely proportional to ω. As a result, the thermal conductivity should have a T^2 trend. However, unlike nanowires or polysilicon, inverse opal has both the effects of surface boundary and grain boundary. Given the T^2 trend at low temperature, there could be two possible explanations. 1, surface scattering is much smaller compared with grain boundary scattering. Effectively, the mean free path at low temperature is determined by grain boundary. 2, surface scattering is also frequency dependent. This is likely to be true for feature size smaller than 50 nm [68]. In this case, one cannot decouple these two effects.

Given the limited sets of data and the coexistence of two scattering mechanisms, it is hard to conclude which assumption is correct. Further study could focus on inverse opals with big shell thickness but small grain size. By doing so, the impact of surface scattering can be reduced as grain boundary scattering would be dominant. Again, to achieve small grains, low temperature annealing is necessary. On the other hand, study on surface scattering

can be carried out with silicon thin films. The dimension should be less than 50 nm, as is in inverse opals. The surface conditions should be carefully characterized, e.g. surface roughness and native oxide. All these conditions could affect the scattering processes.

CHAPTER 4

SUMMARY AND CONCLUSIONS

The efficiency of energy conversion in a thermoelectric material depends on the thermoelectric figure of merit, ZT. A reduction in thermal conductivity enhances the figure of merit for thermoelectric materials. We have shown that similar enhancement in the figure of merit is possible in polysilicon inverse opal. We present a model for charge and thermal transport in highly doped polysilicon inverse opals. Nanoscale grains in addition to the large surface area available for scattering phonons result in a net enhancement in the figure of merit for thermoelectric energy conversion. A surprising result is that a smaller grain size yields a larger ZT. We understand this in terms of the relative impact of nanoscale grains on electron versus phonon transport. We find that by tuning the relationship between shell thickness and grain size, ZT exceeds 0.1 at room temperature and can be as high as 0.6 at 600 K.

We also present the thermal conductivity measurements of 3 different samples. We find that the porous structure exhibits extremely low thermal conductivity (< 2W/mK at room temperature). The thermal conductivity is further reduced with smaller shell thickness. We obtain the intrinsic material thermal conductivity from boundary integral solution to the flow fields. The intrinsic material thermal conductivity can be described by the kinetic theory with effective mean free path. The phonon mean free path is limited by the surface and grain boundaries. The T^2 trend in thermal conductivity at low temperature implies the mean free path is frequency dependent. However, the coexistence of surface and grain boundary scattering complicates the analysis. To decouple these two effects needs more experimental work. The thermal conductivity measurements also suggests that any application that utilizes inverse opal structure (e.g. the emitter in a solar cell) needs careful thermal design, so that overheating is minimized.

Future experimental work could go two directions. To make a realistic thermoelectric

material, one should investigate the fabrication of inverse opals with small grain sizes as well as the possibility of doping the structures in-situ followed by low temperature annealing to preserve grain size. The doping step is critical as the performance of a thermoelectric device is directly affected. To preserve small grains is challenging. On one hand, high temperature is required to recrystalize the structure and remove defects. On the other hand, grains will grow under high temperature, which is not desired for ZT. The condition of annealing should become the emphasis in future work.

To understand the scattering mechanisms, one should make structures that can decouple the two dominant scattering processes at low temperature. Inverse opals with big shell thickness but small grain size could help reduce the impact of surface scattering, as grain boundary scattering would be dominant. Again, to achieve small grains, low temperature annealing is necessary. On the other hand, study on surface scattering can be carried out with silicon thin films. The dimension should be less than 50 nm, as is in inverse opals. Silicon thin films can be released from an SOI wafer. One possible route is to use a suspended platform [68] to measure the thermal conductivity of thin films.

REFERENCES

[1] G. A. Slack, *Solid State Physics*, H. Ehrenreich, F. Seitz, and D. Turnbull, Eds. Academic, New York, 1979.

[2] A. Majumdar, "Thermoelectricity in semiconductor nanostructures," *Science*, vol. 303, no. 5659, pp. 777–778, 2004.

[3] A. Shakouri, "Recent developments in semiconductor thermoelectric physics and materials," *Annual Review of Materials Research*, vol. 41, no. 1, pp. 399–431, 2011.

[4] G. S. Nolas, J. Poon, and M. Kanatzidis, "Recent developments in bulk thermoelectric materials," *MRS Bulletin*, vol. 31, pp. 199–205, 2006.

[5] G. J. Snyder and E. S. Toberer, "Complex thermoelectric materials," *Nature Materials*, vol. 7, pp. 105–114, 2008.

[6] A. Hochbaum, R. Chen, R. D. Delgado, W. Liang, E. C. Garnett, M. Najarian, A. Majumdar, and P. Yang, "Enhanced thermoelectric performance of rough silicon nanowires," *Nature*, vol. 451, pp. 163–167, 2008.

[7] A. I. Boukai, Y. Bunimovich, J. Tahir-Kheli, J.-K. Yu, W. A. Goddard III, and J. R. Heath, "Silicon nanowires as efficient thermoelectric materials," *Nature*, vol. 451, pp. 168–171, 2008.

[8] P. E. Hopkins, C. M. Reinke, M. F. Su, R. H. Olsson, E. A. Shaner, Z. C. Leseman, J. R. Serrano, L. M. Phinney, and I. El-Kady, "Reduction in the thermal conductivity of single crystalline silicon by phononic crystal patterning," *Nano Letters*, vol. 11, no. 1, pp. 107–112, 2011.

[9] J. Tang, H.-T. Wang, D. H. Lee, M. Fardy, Z. Huo, T. P. Russell, and P. Yang, "Holey silicon as an efficient thermoelectric material," *Nano Letters*, vol. 10, no. 10, pp. 4279–4283, 2010.

[10] A. Stein and R. C. Schroden, "Colloidal crystal templating of three-dimensionally ordered macroporous solids: materials for photonics and beyond," *Current Opinion in Solid State and Materials Science*, vol. 5, no. 6, pp. 553 – 564, 2001.

[11] S.-H. Kim, S. Y. Lee, S.-M. Yang, and G.-R. Yi, "Self-assembled colloidal structures for photonics," *NPG Asia Materials*, vol. 3, pp. 25–33, 2011.

[12] J. F. Galisteo-Lopez, M. Ibisate, R. Sapienza, L. S. Froufe-Perez, A. Blanco, and C. Lopez, "Self-assembled photonic structures," *Advanced Materials*, vol. 23, no. 1, pp. 30–69, 2011.

[13] V. L. Colvin, "From opals to optics: Colloidal photonic crystals," *MRS Bulletin*, vol. 26, pp. 637–641, 2001.

[14] J. O. Sofo and G. D. Mahan, "Diffusion and transport coefficients in synthetic opals," *Phys. Rev. B*, vol. 62, pp. 2780–2785, Jul 2000.

[15] J. D. Albrecht, P. A. Knipp, and T. L. Reinecke, "Thermal conductivity of opals and related composites," *Phys. Rev. B*, vol. 63, p. 134303, Mar 2001.

[16] J. C. Maxwell, *A Treatise on Electricity and Magnetism.* Oxford : Clarendon Press, 1873.

[17] R. Landauer, "The electrical resistance of binary metallic mixtures," *Journal of Applied Physics*, vol. 23, no. 7, pp. 779–784, 1952.

[18] J. S. King, E. Graugnard, and C. J. Summers, "Tio2 inverse opals fabricated using low-temperature atomic layer deposition," *Advanced Materials*, vol. 17, no. 8, pp. 1010–1013, 2005.

[19] G. Zeng, J.-H. Bahk, J. E. Bowers, J. M. O. Zide, A. C. Gossard, Z. Bian, R. Singh, A. Shakouri, W. Kim, S. L. Singer, and A. Majumdar, "Eras:(ingaas)[sub 1 - x](inalas)[sub x] alloy power generator modules," *Applied Physics Letters*, vol. 91, no. 26, p. 263510, 2007.

[20] D. G. Cahill, "Thermal conductivity measurement from 30 to 750 k: the 3 omega method," *Review of Scientific Instruments*, vol. 61, no. 2, pp. 802–808, 1990.

[21] T. I. Kamins, "Hall mobility in chemically deposited polycrystalline silicon," *Journal of Applied Physics*, vol. 42, no. 11, pp. 4357–4365, 1971.

[22] G. Baccarani, B. Ricco, and G. Spadini, "Transport properties of polycrystalline silicon films," *Journal of Applied Physics*, vol. 49, no. 11, pp. 5565–5570, 1978.

[23] J. Y. W. Seto, "The electrical properties of polycrystalline silicon films," *Journal of Applied Physics*, vol. 46, no. 12, pp. 5247–5254, 1975.

[24] N.-C. Lu, L. Gerzberg, C.-Y. Lu, and J. Meindl, "Modeling and optimization of monolithic polycrystalline silicon resistors," *Electron Devices, IEEE Transactions on*, vol. 28, no. 7, pp. 818 – 830, jul 1981.

[25] Y. Alpern and J. Shappir, "The temperature dependence of polycrystalline si bulk and surface conductivity," *Journal of Applied Physics*, vol. 64, no. 10, pp. 4987–4992, 1988.

[26] A. McConnell, S. Uma, and K. Goodson, "Thermal conductivity of doped polysilicon layers," *Microelectromechanical Systems, Journal of*, vol. 10, no. 3, pp. 360 –369, sep 2001.

[27] A. F. Mayadas and M. Shatzkes, "Electrical-resistivity model for polycrystalline films: the case of arbitrary reflection at external surfaces," *Phys. Rev. B*, vol. 1, pp. 1382–1389, Feb 1970.

[28] J. E. Palmer, C. V. Thompson, and H. I. Smith, "Grain growth and grain size distributions in thin germanium films," *Journal of Applied Physics*, vol. 62, no. 6, pp. 2492–2497, 1987.

[29] C. Jacoboni and L. Reggiani, "The monte carlo method for the solution of charge transport in semiconductors with applications to covalent materials," *Rev. Mod. Phys.*, vol. 55, pp. 645–705, Jul 1983.

[30] M. V. Fischetti, "Effect of the electron-plasmon interaction on the electron mobility in silicon," *Phys. Rev. B*, vol. 44, pp. 5527–5534, Sep 1991.

[31] H. Brooks, "Scattering by ionized impurities in semiconductors," *Phys. Rev.*, vol. 83, p. 879, 1951.

[32] J. R. Meyer and F. J. Bartoli, "Phase-shift calculation of ionized impurity scattering in semiconductors," *Phys. Rev. B*, vol. 23, pp. 5413–5427, May 1981.

[33] J. Irvin, *Bell Syst. tech. J.*, vol. 41, p. 387, 1962.

[34] F. Mousty, P. Ostoja, and L. Passari, *J. Appl. Phys.*, vol. 45, p. 4576, 1974.

[35] I. Ahmad, A. Omar, and A. Mikdad, "The effect of doping methods on electrical properties and micromorphology of polysilicon gate electrode in submicron cmos devices," *Semiconductor Physics, Quantum Electronics & Optoelectronics*, vol. 5, pp. 188–192, 2002.

[36] M. M. Mandurah, K. C. Saraswat, C. R. Helms, and T. I. Kamins, "Dopant segregation in polycrystalline silicon," *Journal of Applied Physics*, vol. 51, no. 11, pp. 5755–5763, 1980.

[37] F. Demami, R. Rogel, A.-C. Salaun, and L. Pichon, "Electrical properties of polysilicon nanowires for device applications," *physica status solidi (c)*, vol. 8, no. 3, pp. 827–830, 2011.

[38] S. Bouwstra, E. Weerd de, and M. Elwenspoek, "In situ phosphorus-doped polysilicon for excitation and detection in micromechanical resonators," *Sensors and Actuators A: Physical*, vol. 24, no. 3, pp. 227–235, 1990.

[39] M. T. Bjork, H. Schmid, J. Knoch, H. Riel, and W. Riess, "Donor deactivation in silicon nanostructures," *Nature Nanotechnology*, vol. 4, pp. 103–107, 2009.

[40] M. G. Holland, "Analysis of lattice thermal conductivity," *Phys. Rev.*, vol. 132, pp. 2461–2471, Dec 1963.

[41] M. Asen-Palmer, K. Bartkowski, E. Gmelin, M. Cardona, A. P. Zhernov, A. V. Inyushkin, A. Taldenkov, V. I. Ozhogin, K. M. Itoh, and E. E. Haller, "Thermal conductivity of germanium crystals with different isotopic compositions," *Phys. Rev. B*, vol. 56, pp. 9431–9447, Oct 1997.

[42] Z. Wang, J. E. Alaniz, W. Jang, J. E. Garay, and C. Dames, "Thermal conductivity of nanocrystalline silicon: Importance of grain size and frequency-dependent mean free paths," *Nano Letters*, vol. 11, no. 6, pp. 2206–2213, 2011.

[43] M. Asheghi, K. Kurabayashi, R. Kasnavi, and K. E. Goodson, "Thermal conduction in doped single-crystal silicon films," *Journal of Applied Physics*, vol. 91, no. 8, pp. 5079–5088, 2002.

[44] J. Zou and A. Balandin, "Phonon heat conduction in a semiconductor nanowire," *Journal of Applied Physics*, vol. 89, no. 5, pp. 2932–2938, 2001.

[45] M. Lundstrom, *Fundamentals of Carrier Transport*. Cambridge University Press, 2000.

[46] E. M. Conwell, *High Field Transport in Semiconductors*. Academic Press Inc., 1967.

[47] Y. S. Ju and K. E. Goodson, "Phonon scattering in silicon films with thickness of order 100 nm," *Applied Physics Letters*, vol. 74, no. 20, pp. 3005–3007, 1999.

[48] F. Vlklein, "Characterization of the thermal properties of bulk and thin-film materials by using diagnostic microstructures," in *Proceedings of the Symposium on Microtechnology in Metrology and Metrology in Microsystems*, 2000.

[49] C. Herring, "Theory of the thermoelectric power of semiconductors," *Phys. Rev.*, vol. 96, pp. 1163–1187, Dec 1954.

[50] M. W. Wu, N. J. M. Horing, and H. L. Cui, "Phonon-drag effects on thermoelectric power," *Phys. Rev. B*, vol. 54, pp. 5438–5443, Aug 1996.

[51] X. L. Lei, "Thermoelectric power in the balance equation theory," *Journal of Physics: Condensed Matter*, vol. 6, no. 21, p. L305, 1994.

[52] T. H. Geballe and G. W. Hull, "Seebeck effect in silicon," *Phys. Rev.*, vol. 98, pp. 940–947, May 1955.

[53] L. Weber and E. Gmelin, "Transport properties of silicon," *Applied Physics A: Materials Science & Processing*, vol. 53, pp. 136–140, 1991.

[54] H. Casimir, "Note on the conduction of heat in crystals," *Physica*, vol. 5, no. 6, pp. 495 – 500, 1938.

[55] P. A. Beck and P. R. Sperry, *Trans. AIME*, vol. 180, p. 240, 1949.

[56] T. Ishii, T. Osabe, T. Mine, T. Sano, B. Atwood, and K. Yano, "A poly-silicon tft with a sub-5-nm thick channel for low-power gain cell memory in mobile applications," *Electron Devices, IEEE Transactions on*, vol. 51, no. 11, pp. 1805 – 1810, nov. 2004.

[57] J.-Y. Yu, S.-W. Chung, and J. R. Heath, "Silicon nanowires: Preparation, device fabrication, and transport properties," *The Journal of Physical Chemistry B*, vol. 104, no. 50, pp. 11 864–11 870, 2000.

[58] E. C. Nelson, N. L. Dias, K. P. Bassett, S. N. Dunham, V. Verma, M. Miyake, P. Wiltzius, J. A. Rogers, J. J. Coleman, X. Li, and P. V. Braun, "Epitaxial growth of three-dimensionally architectured optoelectronic devices," *Nature Materials*, vol. 10, pp. 676–681, 2011.

[59] T. Suezaki, J. I. L. Chen, T. Hatayama, T. Fuyuki, and G. A. Ozin, "Electrical properties of p-type and n-type doped inverse silicon opals - towards optically amplified silicon solar cells," *Applied Physics Letters*, vol. 96, no. 24, p. 242102, 2010.

[60] M. Arienzo, A. Megdanis, P. Sackles, and A. Michel, "In situ arsenic-doped polysilicon for vlsi applications," *Electron Devices, IEEE Transactions on*, vol. 33, no. 10, pp. 1535 – 1538, oct 1986.

[61] S. Kalainathan, R. Dhanasekaran, and P. Ramasamy, "Grain size and size distribution in heavily phosphorus doped polycrystalline silicon," *Journal of Crystal Growth*, vol. 104, no. 2, pp. 250 – 256, 1990.

[62] W. Stober, A. Fink, and E. Bohn, "Controlled growth of monodisperse silica spheres in the micron size range," *Journal of Colloid and Interface Science*, vol. 26, no. 1, pp. 62 – 69, 1968.

[63] P. Jiang, J. F. Bertone, K. S. Hwang, and V. L. Colvin, "Single-crystal colloidal multilayers of controlled thickness," *Chemistry of Materials*, vol. 11, no. 8, pp. 2132–2140, 1999.

[64] C. Dames and G. Chen, "1 omega, 2 omega, and 3 omega methods for measurements of thermal properties," *Review of Scientific Instruments*, vol. 76, no. 12, p. 124902, 2005.

[65] X. J. Hu, A. A. Padilla, J. Xu, T. S. Fisher, and K. E. Goodson, "3-omega measurements of vertically oriented carbon nanotubes on silicon," *Journal of Heat Transfer*, vol. 128, no. 11, pp. 1109–1113, 2006.

[66] T. Borca-Tasciuc, A. R. Kumar, and G. Chen, "Data reduction in 3 omega method for thin-film thermal conductivity determination," *Review of Scientific Instruments*, vol. 72, no. 4, pp. 2139–2147, 2001.

[67] S. A. Putnam, D. G. Cahill, P. V. Braun, Z. Ge, and R. G. Shimmin, "Thermal conductivity of nanoparticle suspensions," *Journal of Applied Physics*, vol. 99, no. 8, p. 084308, 2006. [Online]. Available: http://link.aip.org/link/?JAP/99/084308/1

[68] D. Li, Y. Wu, P. Kim, L. Shi, P. Yang, and A. Majumdar, "Thermal conductivity of individual silicon nanowires," *Applied Physics Letters*, vol. 83, no. 14, pp. 2934–2936, 2003. [Online]. Available: http://link.aip.org/link/?APL/83/2934/1